The 16th Cambridge Workshop on Cool Stars, Stellar Systems and the Sun
ASP Conference Series, Vol. 448, Electronic Edition
Christopher M. Johns-Krull, Matthew K. Browning, and Andrew A. West, eds.

Coordinated Optical/X-ray Observations of the CTTS V2129 Oph The Chandra View

E. Flaccomio,[1] C. Argiroffi,[1,2] S.H.P. Alencar,[3] J. Bouvier,[4] J.-F. Donati,[5] K. Getman,[6] S. G. Gregory,[7] G. Hussain,[8] M. Ibrahimov,[9] M. M. Jardine,[10] M. Skelly,[5] and F. Walter[11]

[1]*INAF - Osservatorio Astronomico di Palermo, Piazza del Parlamento 1, 90134 Palermo, Italy*

[2]*DSFA - Università degli Studi di Palermo, Piazza del Parlamento, 1, 90134 Palermo, Italy*

[3]*Departamento de Física - ICEx - UFMG, Av. Antonio Carlos, 6627, 30270-901 Belo Horizonte, MG, Brazil*

[4]*Laboratoire d'Astrophysique, Observatoire de Grenoble, BP 53, 38041 Grenoble Cedex 9, France*

[5]*LATT, Universite de Toulouse, CNRS, 14 Av. E. Belin, F-31400 Toulouse, France*

[6]*Department of Astronomy & Astrophysics, 525 Davey Laboratory, Pennsylvania State University, University Park, PA 16802, USA*

[7]*California Institute of Technology, MC 249-17, Pasadena, CA 91125, U.S.A.*

[8]*ESO, Karl-Schwarzschild-Str. 2, D-85748 Garching, Germany*

[9]*Ulugh Bek Astronomical Institute of the Uzbek Academy of Sciences, Astronomicheskaya 33, Tashkent 700052, Uzbekistan*

[10]*School of Physics and Astronomy, University of St Andrews, St Andrews, Scotland KY16 9SS*

[11]*Department of Physics and Astronomy, Stony Brook University, Stony Brook, NY 11794-3800, U.S.A.*

Abstract. Young low-mass accreting stars (classical T Tauri stars; CTTSs) possess strong magnetic fields that are responsible for the regulation of the accretion and outflow processes, and the confinement and heating of coronal plasma. Understanding the physics of CTTS magnetospheres and of their interaction with circumstellar disks can elucidate the history and evolution of our own Sun and Solar System, at the stage when planets were being formed. In June 2009 we have conducted an extensive multi-wavelength observing campaign of V2129 Oph, a K5 CTTS in the ρ Ophiuchi molecular cloud, with the goal of obtaining a synoptic view of its photosphere, magnetic field, coronal plasma, and of its accretion spot(s) and funnel flow(s). We here report on the X-ray emission, as observed by the Chandra High Energy Transmission Grating (HETG). High-density plasma, presumably from the accretion shock, is responsible for the soft X-ray emission, at least during the first half of the observation. The X-ray emission from both the coronal plasma (T~20MK) and the cooler and denser material from the

accretion spot (T∼3MK) is observed to vary between the first and second half of the observation. From the high-resolution X-ray spectra we constrain the emission measure of the two components and the density of the cool plasma. Finally we interpret the time variability of the cool plasma component in terms of stellar rotation and the time-changing viewing angle of the accretion stream, as constrained by simultaneous optical observations.

1. Introduction

V2129 Oph is an optically bright CTTS in the ρ Oph star-forming region. Its brightness, V∼11.2, rotational period, ∼6.5d, and the inclination of its axis to the line of sight, ∼60°, make V2129 Oph a good target for Doppler and Zeeman-Doppler imaging (Donati et al. 2007), allowing the reconstruction of brightness and magnetic field maps that include contributions from the unperturbed photosphere, dark spots, and bright accretion regions ($\dot{M} \sim 10^{-9}\,M_{\odot}yr^{-1}$). V2129 Oph is also one of the few CTTSs that are bright enough in X-rays to perform high-resolution spectroscopy with current X-ray instruments, thus constraining the properties of both the hot coronal X-ray emitting plasma (e.g. the emission measure distribution) and of the cooler X-ray emitting post-accretion-shock material (e.g. emission measure and density).

We have obtained two 100 ksec *Chandra* HETG exposures at two distinct phases during a stellar rotation, simultaneously with an extensive optical monitoring campaign, including multiband-multisite photometry (SMARTS@CTIO, Maidanak Observatory, Palermo Observatory), high-resolution spectroscopy (HARPS@ESO3.6m, SMARTS) and spectro-polarimetry (ESPaDOnS@CFHT). The *Chandra* observation, in addition to augmenting the small sample of young accreting stars with well characterized X-ray properties, give us the unique opportunity to correlate the time-resolved X-ray properties of V2129 Oph with the Zeeman-Doppler brightness and magnetic field maps derived by Donati et al. (2010) from nearly simultaneous observations.

2. The *Chandra* observation

V2129 Oph was observed by *Chandra*/HETGS on 27-29 June 2009, for a total exposure of 200.4 ks. The observation, performed during two consecutive orbits, was divided into two segments with durations of 98.9 and 101.7 ks, and separated by 88.6 ks.

Figure 1 shows the background-subtracted light curve constructed from the arrival times of photons in *source* and *background* regions of both the 0^{th} order image and the HEG and MEG dispersed spectra. The time elapsed since the beginning of the observation and the rotational phase of V2129 Oph (defined as in Donati et al. 2007) are given in the lower and upper x-axis, respectively.

The light curve shows a clear flare toward the middle of the first segment, lasting ∼10 hours and with peak count-rate ∼ 3 times higher than the pre-flare level, and what appears as a smaller flare toward the end of the same segment. During the second segment a seemingly more gradual variability is observed with a slow decay in the first ∼35 ksec, and a similarly slow rise in the last ∼35 ksec.

The upper part of Fig. 1 also shows the accretion shock emission (from the Ca II IR triplet) and the strength of the radial component of the magnetic field in the earth-facing

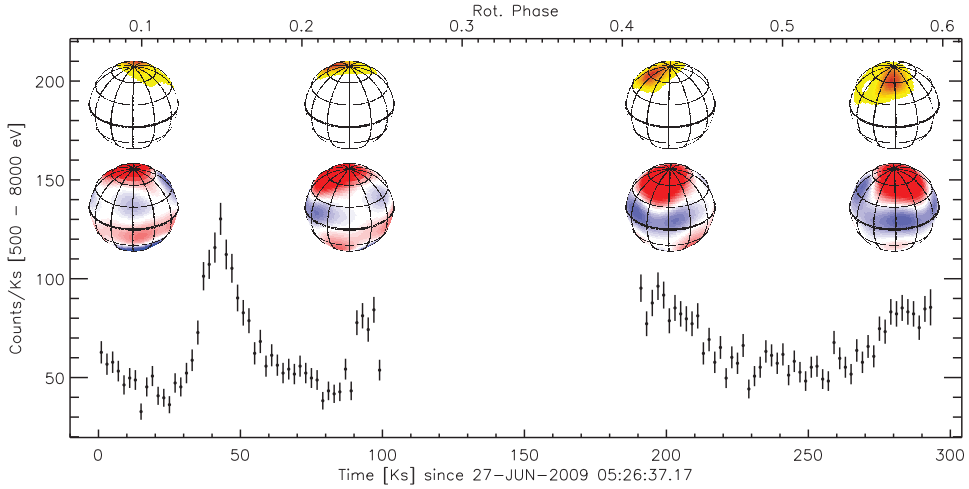

Figure 1. *Chandra* light curve in the 0.5-10.0 keV band combining events from the zero-order image and the HEG and MEG first order spectra, with 2 ks time bin. Shown above the light curve are images of the excess emission due to accretion (upper row) and of the radial component of the magnetic field (lower row) as reconstructed with quasi-simultaneous Zeeman-Doppler imaging by Donati et al. (2010). Colors scales are as in Donati et al. (red and blue in the lower row indicate positive and negative B-fields, respectively). The images refer to rotational phases at the beginning and at the end of each of the two X-ray exposures.

stellar hemisphere at the beginning and at the end of the each of the two *Chandra* exposures, as determined by Donati et al. (2010) from near-simultaneous Zeeman-Doppler imaging.

2.1. Dispersed spectra and long term variability

The dispersed HEG and MEG spectra give access to individual line fluxes allowing a detailed characterization of the X-ray emitting plasma in terms of Differential Emission Measure (*dem*), element abundances, and electron density.

We measured line fluxes and performed our complete spectral analysis separately for the spectra collected during the two observing segments. We therefore explore, with the detail offered by high resolution spectroscopy, variability on time scales of ~ 100 ks. Shorter time scales cannot be investigated with these diagnostic tools because of the limited signal to noise ratio. We also analyzed the spectrum collected during the entire observation so to obtain the time-averaged plasma properties with the highest possible accuracy.

In order to increase the signal to noise ratio we added the MEG and HEG 1^{st} order spectra, having first rebinned the HEG spectra to the MEG wavelength grid. With this procedure we obtained two dispersed spectra, one for each of the two observing segments, totaling 3750 and 4274 net counts, respectively. Figure 1 shows the resulting spectra with labels identifying the strongest emission lines.

We measured the fluxes of the strongest emission lines through direct integration of the binned spectra and subtracting the continuum contribution, estimated from nearby wavelength intervals free of evident emission lines. We also measured the continuum emission of V2129 Oph in wavelength intervals free of significant line contri-

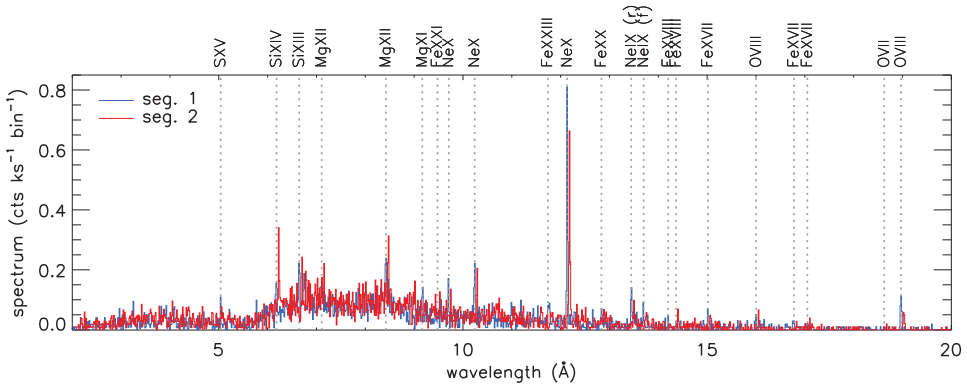

Figure 2. V2129 Oph X-ray spectra observed with *Chandra* (HEG+MEG 1st orders) during the two observing segments. The spectra are rebinned by a factor of 3 (bin size = 0.015 Å), and the spectrum relative to seg. 2 is shifted toward longer wavelengths by 0.05 Å.

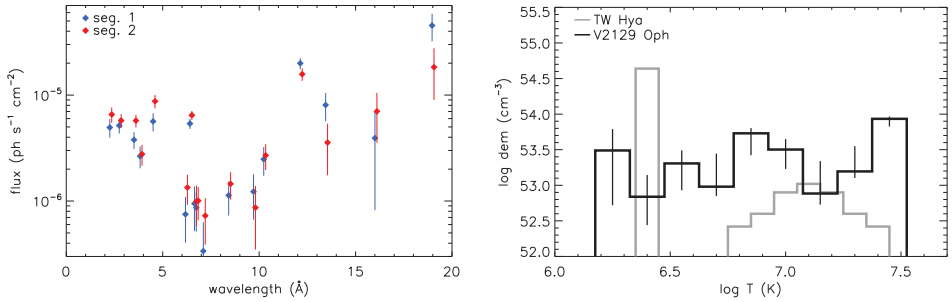

Figure 3. [Left]: Line and continuum fluxes as a function of wavelength. Values measured in the two observing segments are plotted separately. Long wavelength fluxes (i.e. $\lambda > 10$Å) were systematically higher in the first half of the observation, while the opposite is true for fluxes at shorter wavelengths (i.e. $\lambda < 10$Å). [Right:] Differential Emission Measure ($DEM = N_e N_H \Delta V / \Delta \log T$) of V2129 Oph compared to that of TW Hya, as derived by Brickhouse et al. (2010) from a 500ks Chandra/HETGS observation.

butions. Figure 3 (left panel) shows, as a function of wavelength, the measured line and continuum fluxes, separately for the two observing segments. We only plot the fluxes of features detected at the 2σ level in at least one segment.

We note that fluxes at short wavelengths tend to be, on average, higher in seg. 2 than in seg. 1, while the opposite happens for fluxes at long wavelengths. Since shorter wavelength features are, on average, produced by hotter plasma than longer wavelength one, this difference between the two observing segments suggests a difference in the *dem* of the plasma.

2.1.1. Time averaged Differential Emission Measure

We derived the *DEM* and abundances of the plasma responsible for the X-ray emission of V2129 Oph by applying the Markov-Chain Monte Carlo method of Kashyap & Drake (1998) to the measured continuum and line fluxes. For the reconstruction of the

DEM (and abundances) we considered all the measured fluxes discarding only the lines that depend on plasma density, i.e. the intercombination and forbidden lines of He-like triplets.

Starting from the measured fluxes and considering the peak temperature at which each line is produced we reconstructed the *DEM* over a regular logarithmic temperature grid with 0.15 dex bins in the $\log T$ range between 6.2 and 7.5. The resulting *DEM* is shown in Fig. 3 (right panel). Also shown is the *DEM* of TW Hya as derived by Brickhouse et al. (2010) from a 500 ks Chandra/HETGS observation. Note that the *EM* values of bins at the boundary of our temperature domain may be overestimated: artificially limiting the temperature range of the *DEM* reconstruction forces to zero the *DEM* outside this range. Plasma at higher and lower temperatures may however contribute to the measured fluxes, thus causing the *EM* at the boundary bins to be overestimated in order to account for the observed fluxes.

Figure 3 shows that V2129 Oph has larger amounts of hot ($T \geq 10$ MK) plasma than TW Hya, indicating a more active corona. On the other hand the *DEM* of TW Hya shows a sharp peak at 2.5 MK ($\log T = 6.4$), likely produced by material heated in the accretion shock, that is not seen in V2129 Oph. A significant amount of ~2-4MK plasma is anyway also present on V2129 Oph.

2.2. Electron density

The plasma density N_e can be constrained using He-like line triplets, and, in particular, the flux ratio between the intercombination line, *i*, and the forbidden line, *f* (Gabriel & Jordan 1969). Increasing plasma densities result in decreasing f/i ratios.

The only He-like triplets with sufficient signal in our observation is that of Ne IX (13.45, 13.55, and 13.70 Å), with formation temperature ~ 4 MK. It thus provides information on the electron density of plasma at this temperature. Fig. 4 (left) shows the Ne IX triplet observed in the two observing segments. The overall flux of the triplet is clearly lower in the second observing segment than in first. We obtain $f/i = 1.2^{+1.6}_{-0.6}$ and $f/i > 2.3$ for seg. 1 and 2, respectively. The comparison of the observed f/i values with the predicted f/i-ratio vs. plasma density function is shown Fig. 4 (right panel). From this relation we derive: $\log N_e = 12.1^{+0.5}_{-1.0}$ and $\log N_e < 11.5$ for seg. 1 and 2, respectively, with N_e in cm^{-3}.

3. Summary of results

- The Ne IX He-like triplet indicates the presence of cool (~3MK) high-density ($\sim 10^{12} cm^{-3}$) plasma, at least during the first half of the observation (seg. 1).

- This density is not typical of coronal plasma, but compatible with material heated in an accretion shock. Assuming that the resonance line is produced in the accretion shock we estimate, for the first half of the observation, an "X-ray" accretion rate of $\dot{M} = 8.0 \pm 2.4 \times 10^{-11} M_\odot yr^{-1}$ This is a factor of ~10 lower than derived from optical emission lines, similarly to what found for several other CTTSs (e.g. Argiroffi et al. 2009), possibly indicating that we are only observing a fraction of the X-ray emission from the post-shock region.

- The X-ray flux from the cool plasma varies significantly, by a factor of ~2, between the two segments of the observation, corresponding to two different stellar

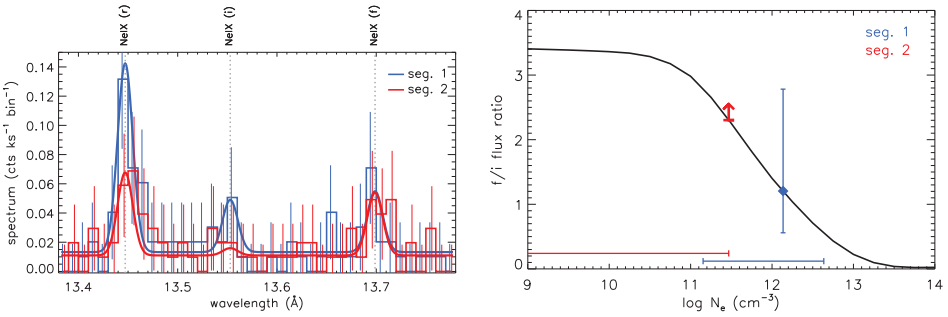

Figure 4. [Left]: Observed spectra in the Ne IX triplet region, shown separately for the two segments of the *Chandra* observation. Labels indicate the three triplet lines (resonance r, intercombination i, and forbidden f). The f/i line ratio is sensitive to the electron density, N_e. [Right]: Line ratio of the forbidden (f) and intercombination (i) lines of the Ne IX triplet. The black curve indicates the predicted ratios for different electron densities, N_e. Line ratios measured in the two segments, and the corresponding inferred densities, are marked in red and blue. For seg. 2, due to the lower line fluxes, we only obtain a lower limit for the f/i ratio, and an upper limit for the density.

rotation phases and, therefore, viewing geometries of the accretion shock. These geometries are well constrained by simultaneous optical Zeeman-Doppler imaging, as shown in Fig. 1.

- The time-variability of the cool plasma component may be explained by obscuration of the post-shock region by the associated accretion stream, i.e. if we observe a larger fraction of the shocked plasma emission when the accretion stream hides a smaller fraction of its foot-point. For our observation this could easily occur in segment 1, during which the line of sight to the accretion shock likely intercepts a smaller column density with respect to segment 2. The residual but possibly significant absorption due to the accretion flow might explain the discrepancy between the X-ray and the optically derived mass accretion rates.

Acknowledgments. E.F. and C.A. acknowledge the support of the ASI/INAF agreement I/099/10/0.

References

Argiroffi, C., Maggio, A., Peres, G., Drake, J. J., López-Santiago, J., Sciortino, S., & Stelzer, B. 2009, A&A, 507, 939. 0909.0218

Brickhouse, N. S., Cranmer, S. R., Dupree, A. K., Luna, G. J. M., & Wolk, S. 2010, ApJ, 710, 1835. 1001.0750

Donati, J., Bouvier, J., Walter, F., Gregory, S., Skelly, M., Hussain, G., Flaccomio, E., Argiroffi, C., Grankin, K., Jardine, M., Menard, F., Dougados, C., Romanova, M., & the MaPP collaboration 2010, ArXiv e-prints. 1011.4789

Donati, J., Jardine, M. M., Gregory, S. G., Petit, P., Bouvier, J., Dougados, C., Ménard, F., Cameron, A. C., Harries, T. J., Jeffers, S. V., & Paletou, F. 2007, MNRAS, 380, 1297. 0709.1414

Gabriel, A. H., & Jordan, C. 1969, MNRAS, 145, 241

Kashyap, V., & Drake, J. J. 1998, ApJ, 503, 450